Port-Hamiltonian modeling of large scale curling HASEL actuators ⋆

Cristobal Ponce [*,**], **Nelson Cisneros** [*], **Yongxin Wu** [*], **Kanty Rabenorosoa** [*], **Yann Le Gorrec** [*], **Hector Ramirez** [**]

[*] *FEMTO-ST institute, UBFC, CNRS, Besançon, France.(emails: nelson.cisneros@femto-st.fr,cristobal.ponce@femto-st.fr, yongxin.wu@femto-st.fr, rkanty@femto-st.fr, legorrec@femto-st.fr)*
[**] *Departamento de Electrónica, Universidad Técnica Federico Santa María, Valparaíso, Chile. (email: cristobal.ponces@usm.cl, hector.ramireze@usm.cl)*

Abstract: This paper presents a modeling methodology to enhance the dynamic performance of the mechanical component of finite-dimensional curling HASEL (Hydraulically Amplified Self-Healing Electrostatic) actuators within the port-Hamiltonian systems framework. The proposed approach entails replacing the sheet dynamics that limit deformation in a low-scale model with those derived from a large-scale discretized beam model. By making a few additional assumptions compared to the original low-scale HASEL model, the resulting interconnected system is established by aligning the states of the mechanical component in the low-scale model with those of the large-scale beam model in a straightforward manner. To validate the effectiveness of the methodology, simulated examples are provided along with a comparison to experimental results.

Keywords: Port-Hamiltonian systems; Modeling; HASEL actuator; Soft actuator.

1. INTRODUCTION

Hydraulically Amplified Self-Healing Electrostatic (HASEL) actuators represent a breakthrough in soft robotics, combining elements of dielectric elastomer actuators (DEA) and fluid-driven actuators. Operating as artificial muscles powered by electric fields, HASEL exhibits remarkable resilience to electrical failure, enabling operation at higher voltages compared to DEA. Various applications, including soft grippers and artificial muscle-driven arms, have been explored, as detailed in (Acome et al., 2018). Curling HASEL actuators enable complex bending motions, as demonstrated in (Kellaris et al., 2021) with a spider-inspired robot's legs. Another notable application involves a gripper inspired by an eagle's foot, powered by HASEL actuators mounted on a drone, as presented in (Kim and Cha, 2021). Addressing modeling challenges, (Hainsworth et al., 2022) develops a nonlinear reduced-order model, while (Volchko et al., 2022) presents a linear model for control design in HASEL-powered arms. These advancements highlight the diverse capabilities and potential applications of HASEL technology in the field of soft robotics.

Integrating HASEL actuators with beams offers distinct advantages in continuous and soft robot applications. When coupled with HASEL actuators, the inherent flexibility of beams results in a system capable of executing complex motions with precise control. This enables enhanced adaptability and dynamic response in continuous robotic structures. The port-Hamiltonian systems (PHS) offer a geometric framework for describing interconnected systems. Notable features include power flow between subsystems, separating interconnecting structure from constitutive relationships, and leveraging this structure for analysis and control (Duindam et al., 2009). In (Cisneros et al., 2024), the modeling and control of a curling HASEL actuator is addressed using the port-Hamiltonian (PH) approach. Employing a modular strategy, the HASEL actuator is conceptualized as an interconnection of elementary subsystems. Each subsystem is depicted as an electrical component comprising a parallel capacitor and inductor connected to a mechanical structure consisting of linear and torsional springs. The zipping of electrodes induced by applying high voltage and volume conservation within the fluid chambers enables the coupling between the mechanical and electrical components. Currently, the state of the art regarding modeling and discretization of beams within the PHS framework covers linear and nonlinear models such as Timoshenko beam (Macchelli and Melchiorri, 2004) and Euler-Bernoulli beam (Brugnoli et al., 2021), the cases where is considered piezo-actuation (Voss et al., 2008; Voß and Scherpen, 2014), among others.

The contribution of this paper is a methodology to build PHS of large-scale curling HASEL models suitable for control design and soft-robotic applications. In the proposed approach, the dynamics of the sheet that restricts the deformation is replaced by a discretized beam model.

⋆ The first author acknowledges financial support from ANID/ Becas/ Doctorado Nacional/ 2021-21211290 (Chile) and the ISITE-BFC project - CPHS2D (France). The second and third authors acknowledge EIPHI Graduate School (contract ANR-17-EURE-0002). The fifth author acknowledges the MSCA Project MODCONFLEX 101073558 and the ANR Project IMPACTS ANR-21-CE48-0018.

Then, by aligning the states related to volume conservation in the fluid chambers, the coupled system mirrors that of the original low-scale model. The paper is structured as follows: Section 2 presents background on PHS, the low-scale curling HASEL model, and discretized beam models. Section 3 presents the methodology for coupling. Section 4 presents the identification of parameters and experimental validation. Finally, Section 5 gives some conclusions and discusses future work.

2. PH MODELING OF ELEMENTARY COMPONENTS

This section aims to establish the groundwork for the forthcoming discussion by elucidating fundamental concepts and previous research relevant to PHS, a particular model of the curling HASEL actuator, and discretized beam models.

According to (van der Schaft, 2000), the finite-dimensional PHS model of a physical system can be written as:

$$\begin{aligned} \dot{x} &= [J(x) - R(x)]\nabla_x H(x) + g(x)u \\ y &= g(x)^\top \nabla_x H(x) \end{aligned} \tag{1}$$

with $x \in \mathbb{R}^n$ the state vector, $H(x) > 0 \in \mathbb{R}$ the total energy function called Hamiltonian, $J(x) = -J(x)^\top \in \mathbb{R}^{n\times n}$ the interconnection matrix, $R(x) = R(x)^\top \geq 0 \in \mathbb{R}^{n\times n}$ the dissipation matrix, $g(x) \in \mathbb{R}^{n\times m}$ the input map matrix, and $u, y \in \mathbb{R}^m$ the power-conjugated input and output vectors, respectively. The energy balance equation of PHS can be calculated as

$$\dot{H} = -(\nabla_x H)^\top R \nabla_x H + y^\top u \leq y^\top u$$

indicating that PHS is passive with respect to the storage function $H(x)$.

2.1 Low-scale curling HASEL model

The PH model of the curling HASEL actuator presented here is the one introduced in (Cisneros et al., 2024). This model is structured as an interconnected arrangement of ℓ fundamental subsystems, each consisting of mechanical and electrical components and a hydraulic component through the conservation of volume in the chamber. As shown in Figure 1, the mechanical part is characterized by a lumped mass m_i, the integration of linear springs representing the stiffness K_l^i of the upper layer, and torsional springs representing the stiffness K_f^i of the strain-limiting layer and the resistance of the fluid. The electrical part incorporates a resistance R_i and a variable capacitor C_i representing the electrodes. Additionally, an electrical resistance r_i and an inductance L_i are included in parallel with the capacitor to account for the drift effect, gradually discharging the capacitor over time.

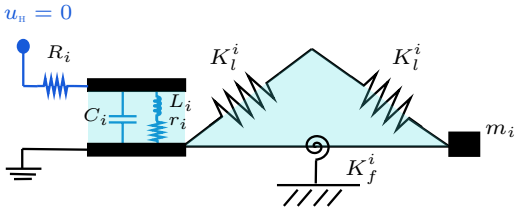

Fig. 1. Scheme of the i-th chamber, with $i = \{1, \ldots, \ell\}$.

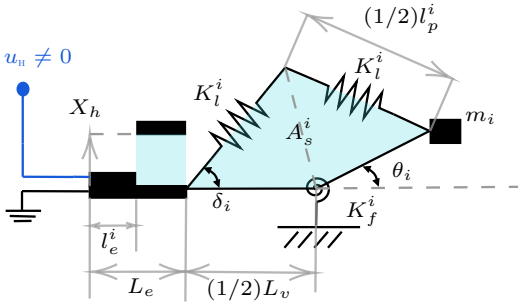

Fig. 2. With the application of high voltage, the electrodes undergo partial zipping, causing the deformation.

To mathematically describe the actuator, we consider the width, denoted by w, to be constant. Thus, geometric analysis for volume conservation is conducted in the plane. Each i-th chamber is conceived as two compartments facilitating fluid exchange. In the equilibrium configuration (when applied voltage $u_н$ set to zero), the active compartment relative to the electrodes is regarded as a rectangle with an initial base length L_e and constant height X_h. Conversely, the passive compartment is modeled as an isosceles triangle with a constant base length L_v, sides of initial length L_p, and an internal angle δ_i. Upon applying a non-zero voltage $u_н$, the electrodes contract to a length l_e^i, leading to fluid displacement from the active to the passive compartment. This action induces an angular deformation θ_i alongside variations in the triangle's side lengths l_p^i and internal angle. To ensure volume conservation, it is assumed that the linear springs elongate uniformly the same magnitude $\varepsilon_i = (l_p^i - L_p)/2$ at any given instant. Moreover, the total volume $V_T = w \cdot A_T$ remains constant, where A_T denotes the total area in the plane, expressed as

$$A_T = A_s^i + X_h(L_e - l_e^i), \tag{2}$$

$$A_s^i(\theta_i, l_p^i) = \frac{1}{4} L_v l_p^i \sin(\delta_i(\theta_i, l_p^i)), \tag{3}$$

$$\delta_i(\theta_i, l_p^i) = \frac{\pi + \theta_i}{2} - \sin^{-1}\left(\frac{L_v}{l_p^i}\sin\left(\frac{\pi - \theta_i}{2}\right)\right), \tag{4}$$

from which it follows that the contracted length l_e^i of the electrodes is given by

$$l_e^i(\theta_i, l_p^i) = \left(L_e - \frac{A_T}{X_h}\right) + \frac{L_v}{4X_h} l_p^i \sin\left(\delta_i(\theta_i, l_p^i)\right). \tag{5}$$

The low-scale PHS model of the curling HASEL actuator proposed in (Cisneros et al., 2024) is given by

$$\underbrace{\begin{bmatrix} \dot{p}_\theta \\ \dot{\theta} \\ \hline \dot{l}_p \\ \dot{\phi} \\ \dot{Q} \end{bmatrix}}_{\dot{x}_н} = \underbrace{\left[\begin{array}{cc|ccc} -b & -I_\ell & -d & 0 & 0 \\ I_\ell & 0 & 0 & 0 & 0 \\ \hline d & 0 & 0 & 0 & 0 \\ 0 & 0 & 0 & -r & I_\ell \\ 0 & 0 & 0 & -I_\ell & -R_e^{-1} \end{array}\right]}_{J_н(x_н) - R_н(x_н)} \underbrace{\begin{bmatrix} \nabla_{p_\theta} H_н \\ \nabla_\theta H_н \\ \hline \nabla_{l_p} H_н \\ \nabla_\phi H_н \\ \nabla_Q H_н \end{bmatrix}}_{\nabla_{x_н} H_н} + \underbrace{\begin{bmatrix} 0 \\ 0 \\ \hline 0 \\ 0 \\ \Gamma_н \end{bmatrix}}_{G_н(x_н)} u_н \tag{6}$$

$$y_н = G_н(x_н)^\top \nabla_{x_н} H_н$$

where $\theta = [\theta_1 \ \ldots \ \theta_\ell]^\top$ is the vector that gathers all the angles of each chamber, analogously the same for $l_p = [l_p^1 \ \ldots \ l_p^\ell]^\top$, $\phi = [\phi_1 \ \ldots \ \phi_\ell]^\top$ and $Q = [Q_1 \ \ldots \ Q_\ell]^\top$, with ϕ_i the magnetic flux and Q_i the electrical charge. The angular momentum variable is defined as $p_\theta = M_н \dot{\theta}$

where $M_{\text{н}} \in \mathbb{R}^{\ell\times\ell}$ is the mass matrix of the actuator. The matrix $b \in \mathbb{R}^{\ell\times\ell}$ represents the mechanical damping of the actuator, $I_\ell \in \mathbb{R}^{\ell\times\ell}$ is the identity matrix, $d(l_p,\theta) = \text{diag}\{\frac{2A_s^1}{l_p^1},\dots,\frac{2A_s^\ell}{l_p^\ell}\} \in \mathbb{R}^{\ell\times\ell}$ is the coupling matrix related to the conservation of volume, $r = \text{diag}\{r_1,\dots,r_\ell\} \in \mathbb{R}^{\ell\times\ell}$ and $R_e = \text{diag}\{R_i,\dots,R_\ell\} \in \mathbb{R}^{\ell\times\ell}$ are resistance matrices associated with the drift effect and the equivalent electric circuit, respectively. Defining $z = [l_p^\top \ \phi^\top \ Q^\top]^\top$ as the state vector related to the electromechanical coupling, the Hamiltonian $H_{\text{н}}(x_{\text{н}})$ of the actuator can be expressed as

$$H_{\text{н}}(x_{\text{н}}) = H_{\text{н}}^m(p_\theta,\theta) + H_{\text{н}}^{em}(z,\theta), \tag{7}$$

where $H_{\text{н}}^m$ is the mechanical part related to the strain-limiting layer and the fluid's resistance, and $H_{\text{н}}^{em}$ is the electromechanical part. Both are given by

$$H_{\text{н}}^m(p_\theta,\theta) = \frac{1}{2}p_\theta^\top M_{\text{н}}^{-1}p_\theta + \frac{1}{2}\theta^\top K_f\theta \tag{8}$$

$$H_{\text{н}}^{em}(z,\theta) = \frac{1}{4}(l_p - L_p)^\top K_l(l_p - L_p) + \frac{1}{2}\phi^\top L_{ind}^{-1}\phi \ \dots \\ \cdots + \frac{1}{2}Q^\top C(\theta,l_p)^{-1}Q \tag{9}$$

where $K_f = \text{diag}\{K_f^1,\dots,K_f^\ell\} \in \mathbb{R}^{\ell\times\ell}$ is the stiffness matrix of the strain-limiting layer and the resistance of the fluid, $K_l = \text{diag}\{K_l^1,\dots,K_l^\ell\} \in \mathbb{R}^{\ell\times\ell}$ is the stiffness matrix of the upper layer, $L_{ind} = \text{diag}\{L_1,\dots,L_\ell\} \in \mathbb{R}^{\ell\times\ell}$ is the inductance matrix, and $C(\theta,l_p) = \text{diag}\{C_1,\dots,C_\ell\} \in \mathbb{R}^{\ell\times\ell}$ is the capacitance matrix, with C_i defined as

$$C_i(\theta_i,l_p^i) = \frac{\epsilon_0\epsilon_r w l_e^i(\theta_i,l_p^i)}{2h_f} + \frac{\epsilon_0\epsilon_r w(L_e - l_e^i(\theta_i,l_p^i))}{2h_f + X_h}, \tag{10}$$

with h_f the thickness of the film, ϵ_0 and ϵ_r the vacuum and relative permittivity, respectively. Finally, the input matrix $\Gamma_{\text{н}} \in \mathbb{R}^{\ell\times 1}$ is defined as

$$\Gamma_{\text{н}} = \begin{bmatrix} 1/R_1 & \cdots & 0 \\ \vdots & \ddots & \vdots \\ 0 & \cdots & 1/R_\ell \end{bmatrix} \begin{bmatrix} \alpha\cos(\beta\theta_1) \\ \vdots \\ \alpha\cos(\beta\theta_\ell) \end{bmatrix} = R_e^{-1}\gamma(\theta) \tag{11}$$

where $\alpha \in \mathbb{R}$ and $\beta \in \mathbb{R}$ are constant parameters to be identified experimentally.

2.2 Discretized beam models

In classical infinite-dimensional beam models as the one illustrated in Figure 3, the typical unknowns include the transverse deflection $v_0(\zeta_1,t)$, describing the vertical position of the beam at a point along the neutral axis, as well as the horizontal displacement $u_0(\zeta_1,t)$, and the rotation $\psi(\zeta_1,t)$, representing the inclination of the cross-section. These variables are commonly known as generalized displacements and are the primary unknowns of the system.

The dynamic equations of the system, stem from the equilibrium of linear and angular momentum. Various representations of these models are available in the literature, with PHS formulations being particularly relevant for this study. To obtain large-scale discretized models of beams, various methods have been developed, including the Finite Element Method (FEM) in both its standard and mixed formulations. For a comprehensive review of these methods see (Zienkiewicz et al., 2005). The key steps in obtaining these approximations involve first defining and dividing the beam's geometry into finite elements. Subsequently, degrees of freedom ($\hat{u}_0^k$, $\hat{v}_0^k$, $\hat{\psi}^k$) are assigned to each node of the finite element mesh, enabling the representation of generalized displacements at these points (see Figure 4 for the illustration). Then, an interpolation function is selected to approximate the unknowns, and the approximated model is obtained through spatial integration over each finite element and an assembly process.

Remark 1 Note that to preserve the PH structure in the discrete model, structure-preserving methods must be applied. It is worth mentioning that for infinite-dimensional beam models written as PHS, the states associated with the kinetic energy are generalized momentum $p(\zeta_1,t)$, and those associated with the elastic potential energy are generalized strains $\epsilon(\zeta_1,t)$. By applying structure-preserving methods, the states of the resulting large-scale finite-dimensional PHS has the same physical interpretation. See e.g. (Wang et al., 2017; Warsewa et al., 2021).

For the purposes of this work, the discretized models used in upcoming sections are based on the standard FEM, since this method allows to preserve the structure of the second-order classical Lagrangian representation and the generalized displacements as states. Then, the PHS can be built by means of a change of variables. For completeness, we denote the PHS representation of the large-scale beam model as

$$\dot{\hat{x}}_b = [\hat{J}_b(\hat{x}_b) - \hat{R}_b(\hat{x}_b)]\nabla_{\hat{x}_b}\hat{H}_b + \hat{G}_b(\hat{x}_b)\hat{u}_b \tag{12}$$
$$\hat{y}_b = \hat{G}_b(\hat{x}_b)^\top\nabla_{\hat{x}_b}\hat{H}_b$$

where the hat notation signifies that the variable originates from a discretization process.

3. COUPLING METHODOLOGY

This section outlines a methodology for constructing a large-scale model of a curling HASEL actuator formulated as a PHS. The approach involves substituting the dynamics of the sheet that constrains deformation in a low-scale model with the dynamics of a large-scale discretized beam model. This method enhances the representation of the deformation profile by increasing the number of degrees of freedom describing the system. Additionally, employing the constitutive law within the beam model enables a more accurate representation of the sheet's material properties.

The assumptions used in the proposed methodology are the following:

a) Similar to (6), the discretized PH beam model (12) must include angular momentum and angular deformation as state variables.

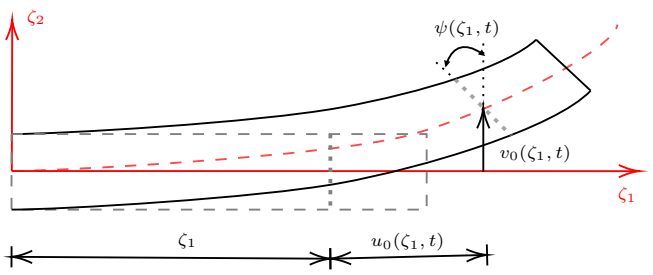

Fig. 3. Beam scheme.

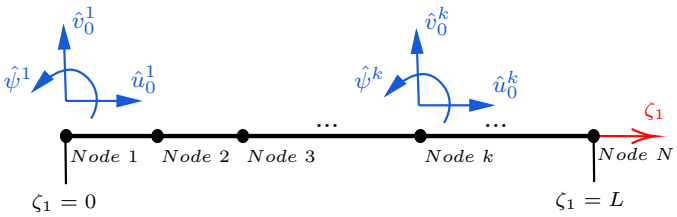

Fig. 4. Mesh, nodes and degrees of freedom.

b) The volume conservation in the chambers is evaluated with respect to a subset of the angular deformation state, and the correction factor $\eta = \text{diag}\{\eta_1, \dots, \eta_\ell\} \in \mathbb{R}^{\ell\times\ell}$ is introduced, which is premultiplied to the coupling term $d(l_p, \theta) \in \mathbb{R}^{\ell\times\ell}$ in (6).

c) In the resulting large-scale model, the stiffness matrix $K_f \in \mathbb{R}^{\ell\times\ell}$ exclusively represents the fluid resistance, and its energy is considered as quadratic with respect to the same subset of the angular deformation state used in the evaluation of volume conservation.

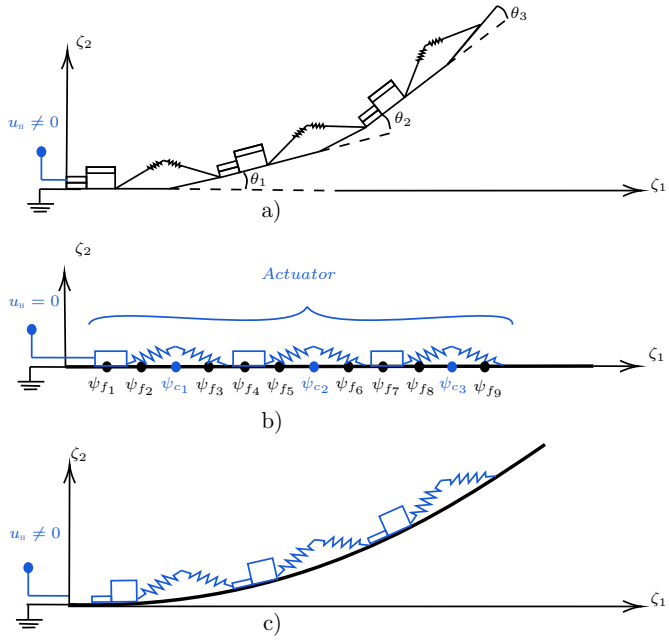

Fig. 5. a) Low-scale actuator b) Large-scale actuator ($u_{\text{H}} = 0$). c) Large-scale actuator ($u_{\text{H}} \neq 0$).

Following the assumption a), suppose that the state of the beam model (12) is organized as follows:

$$\hat{x}_b = \begin{bmatrix} \cdots & \hat{p}_\psi^\top & \cdots & \hat{\psi}^\top & \cdots \end{bmatrix}^\top \tag{13}$$

where $\hat{p}_\psi$ and $\hat{\psi}$ represent the discrete angular momentum and discrete angular deformation state vectors, respectively. Following assumption b), suppose that $\hat{p}_\psi$ and $\hat{\psi}$ are partitioned as

$$\hat{p}_\psi = \begin{bmatrix} \hat{p}_{\psi_f} \\ \hat{p}_{\psi_c} \end{bmatrix}, \quad \hat{\psi} = \begin{bmatrix} \hat{\psi}_f \\ \hat{\psi}_c \end{bmatrix} \tag{14}$$

where $\hat{\psi}_c \in \mathbb{R}^\ell$ is the vector that collects all the angles associated with the nodes at the center positions of the chambers and is used to assess volume conservation. The vector $\hat{\psi}_f$ gathers all other *free* angles (not connected to volume conservation), and $\hat{p}_{\psi_c} \in \mathbb{R}^\ell$ and $\hat{p}_{\psi_f}$ represent their respective angular momenta (see Figure 5.b for an illustrative scheme). To link the coupling terms due to volume conservation in the chambers with the rest of the beam dynamics, the following coupling matrix Σ is defined:

$$\begin{bmatrix} \vdots \\ \hat{p}_{\psi_c} \\ \vdots \end{bmatrix} \rightarrow \quad \Sigma = \begin{bmatrix} 0 \\ [\eta\, d(l_p, \theta)\ 0\ 0] \\ 0 \end{bmatrix}_{\theta=\hat{\psi}_c} \tag{15}$$

where the nonzero rows of Σ are related to the $\hat{p}_{\psi_c}$ coordinates.

Definition 1 The large-scale PH model of the curling HASEL actuator is given by

$$\underbrace{\left[\begin{array}{c|c} \dot{\hat{x}}_b \\ \hline \dot{z} \end{array}\right]}_{\dot{x}} = \underbrace{\left[\begin{array}{c|c} \hat{J}_b - \hat{R}_b & -\Sigma \\ \hline \Sigma^\top & \Lambda_{\text{H}} \end{array}\right]}_{J(x)-R(x)} \underbrace{\left[\begin{array}{c} \nabla_{\hat{x}_b} H \\ \hline \nabla_z H \end{array}\right]}_{\nabla_x H} + \underbrace{\left[\begin{array}{c|c} \hat{G}_b & 0 \\ \hline 0 & \Gamma \end{array}\right]}_{G(x)} \underbrace{\left[\begin{array}{c} \hat{u}_b \\ \hline u_{\text{H}} \end{array}\right]}_{u} \tag{16}$$

$$y = G(x)^\top \nabla_x H$$

with Hamiltonian $H(x)$ given by

$$H(x) = \hat{H}(\hat{x}_b) + H_{\text{H}}^{em}(z, \theta = \hat{\psi}_c) + \frac{1}{2}\hat{\psi}_c^\top K_f \hat{\psi}_c \tag{17}$$

and the matrices Λ_{H} and Γ defined as

$$\Lambda_{\text{H}} = \begin{bmatrix} 0 & 0 & 0 \\ 0 & -r & I_\ell \\ 0 & -I_\ell & -R_e^{-1} \end{bmatrix}, \qquad \Gamma = R_e^{-1}\gamma(\theta = \hat{\psi}_c) \tag{18}$$

where the matching $\theta = \hat{\psi}_c$ is executed component by component and in relation to the corresponding chamber.

Remark 2 Note that the model proposed in Definition 1 is formulated with respect to a generic beam model of arbitrary dimension, which depends solely on the number of nodes employed in discretization. Additionally, it may incorporate nonlinearities and allow mechanical inputs $\hat{u}_b$, representing an improvement over the original low-scale model.

To validate and illustrate the methodology, we choose the Euler-Bernoulli beam model without distributed inputs as an example. Its infinite-dimensional PH representation is given by

$$\underbrace{\begin{bmatrix} \dot{p} \\ \dot{\epsilon} \end{bmatrix}}_{\dot{x}_b} = \underbrace{\begin{bmatrix} 0 & -\partial_1^2 \\ \partial_1^2 & 0 \end{bmatrix}}_{\mathcal{J}_b} \underbrace{\begin{bmatrix} e_p \\ e_\epsilon \end{bmatrix}}_{\delta_{x_b} H_b} \tag{19}$$

$$u_\partial = [e_p(0) \ -\partial_1 e_p(0)\ e_q(L)\ \partial_1 e_\epsilon(L)]^\top$$
$$y_\partial = [\partial_1 e_\epsilon(0)\ e_q(0)\ \partial_1 e_p(L)\ -e_p(L)]^\top$$

associated with a Hamiltonian function $H_b(x_b)$ as

$$H_b(x_b) = \frac{1}{2}\int_0^L \left(\frac{p^2}{\rho A} + EI\epsilon^2\right) d\zeta_1 \tag{20}$$

where $\partial_1^j = \partial^j/\partial\zeta_1^j$, $p(\zeta_1, t) = \rho A \partial v_0/\partial t$ is the linear momentum with ρ the density of the material and A the cross section area, $\epsilon(\zeta_1, t) = \partial_1^2 v_0$ is the the generalized bending strain. The beam length is L, the mass per unit length is ρA, and the beam's bending stiffness is EI, with E Young's modulus and I the second moment of

inertia of the cross-section. The notation $\delta_{x_b} H_b$ represents the variational derivative of H_b respect to $x_b(\zeta_1, t)$. The boundary inputs $u_\partial = 0$ give the boundary conditions corresponding to an end fixed at $\zeta_1 = 0$ and the free one at $\zeta_1 = L$.

Using the standard FEM, the discretized Euler-Bernoulli beam model written as PHS is given by

$$\underbrace{\begin{bmatrix}\dot{\hat{p}}\\ \dot{\hat{q}}\end{bmatrix}}_{\dot{\hat{x}}_b} = \underbrace{\begin{bmatrix}-\hat{D} & -\hat{I}\\ \hat{I} & 0\end{bmatrix}}_{\hat{J}_b - \hat{R}_b} \underbrace{\begin{bmatrix}\hat{M}_b\hat{p}\\ \hat{K}_b\hat{q}\end{bmatrix}}_{\nabla_{\hat{x}_b}\hat{H}_b} + \underbrace{\begin{bmatrix}\hat{B}\\ 0\end{bmatrix}}_{\hat{G}_b} \hat{u}_b \tag{21}$$

with Hamiltonian $\hat{H}_b(\hat{x}_b)$ given by

$$\hat{H}_b(\hat{x}_b) = \frac{1}{2}\hat{p}^\top \hat{M}_b^{-1}\hat{p} + \frac{1}{2}\hat{q}^\top \hat{K}_b \hat{q} \tag{22}$$

being $\hat{M}_b$ the discrete mass matrix, $\hat{K}_b$ the discrete stiffness matrix, $\hat{I}$ an identity matrix of appropriate dimension, and $\hat{D}$ the damping matrix, which is considered as a Rayleigh damping matrix defined as $\hat{D} = a_M \hat{M}_b + a_K \hat{K}_b$, with a_M and a_K two real constants to be determined experimentally.

Remark 3 In the Euler-Bernoulli beam model, it is important to note that the variable u_0 is not included, and ψ is defined as $\partial_1 v_0$. Consequently, the state vector $\hat{q} = [\hat{v}_0^\top \ \hat{\psi}^\top]^\top$ encompasses all degrees of freedom related to vertical and angular deformation, while $\hat{p} = [\hat{p}_{v_0}^\top \ \hat{p}_\psi^\top]^\top$ represents their corresponding momenta.

4. MODEL IDENTIFICATION AND VALIDATION

In this section, the proposed methodology is validated through a two-step process. Firstly, the model's unknown parameters are identified using data from a real system. Subsequently, the model's validity is assessed by comparing simulations with experimental results. The experimental setup features a HASEL C-Series actuator (C-5015-06-01-B-ACAC-50-096) from Artimus Robotics coupled with a strain constrain layer. The Keyence LJ-V7080 laser sensor monitors the position of the tip actuator, and the data is acquired using the dSPACE card CLP1104. The Trek model 610E amplifier supplies power for the actuator (see Fig. 6).

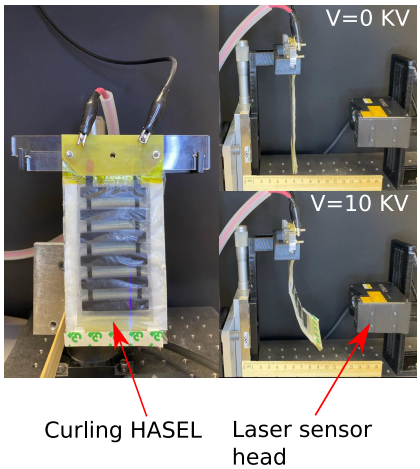

Fig. 6. Experimental setup of curling HASEL actuator.

Table 1. Parameters of the large-scale model.

Symbol	Value	Units	Definition
L_p	0.015	m	Length of top film
L_v	0.01	m	Length of bottom film
L_e	0.01	m	Length of electrodes
X_h	0.002	m	Chamber high
ϵ_r	2.2	F/m	Relative permittivity
ϵ_0	8.854×10^{-12}	F/m	Vacuum permittivity
w	0.075	m	Actuator width
h_f	$18 \times 10^{-}6$	m	Film thickness
R_i	10	Ω	Resistance
r_i	20	Ω	Resistance
L_i	140	F	Inductance
K_l^i	400	N/m	Stiffness
K_f^i	3	Nm/rad	Stiffness
α	30.5	-	Gain parameter
β	2.4	-	Gain parameter
η	diag(0.1, 0.28, ... 0.46, 0.64, 0.82, 1)	-	Correction factors
h	0.2×10^{-3}	m	Height
L	0.12	m	Beam length
A	1.5×10^{-5}	m^2	Area
I	5×10^{-14}	m^4	Cross-section inertia
ρ	2000	Kg/m^3	Density
E	2.66×10^7	Pa	Young's modulus
a_M	5×10^{-6}	-	Damping coefficient
a_K	2.28×10^{-2}	-	Damping coefficient

To characterize the model, the parameters L_i, a_M, a_K, K_f, α, and β are identified, as they have a great impact on the system's dynamics among the group of unmeasurable parameters. Table 1 lists the rest of the parameters. Given that the length of each chamber is $L_e + L_v$, and the center of the triangular compartment is at $L_e + L_v/2$, the beam model is discretized by placing a node at the following coordinates: nodes = [0 0.015 0.021 0.035 0.041 0.055 0.061 0.075 0.081 0.095 0.101 0.115 0.12]. It is worth mentioning that the discretization mesh is not arbitrary. For the presented example, placing a node exactly at the intersection points between chambers apparently results in a singularity somewhere. To address this issue, nodes at the intersections between chambers are shifted a small distance of 0.001 m. Detailed analysis of the origin of this numerical error and sensitivity of the results with different discretization meshes constitute future work and are not covered in this study.

With all the aforementioned information and using the Levenberg-Marquardt optimization algorithm, the unknown parameters are identified using the data acquired from the tip's vertical displacement. The comparison between the measured and modeled tip positions with the identified parameters is presented in Fig. 7, where the input is positive, yielding a fitness percentage of 87.24%.

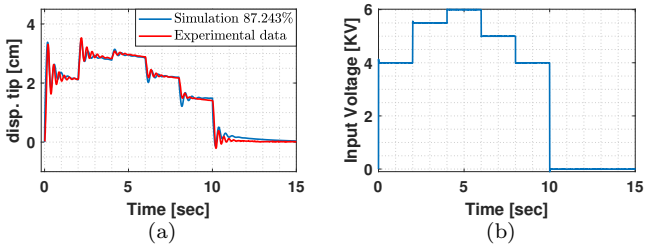

(a) (b)

Fig. 7. (7a) Model identification (7b) Positive input signal.

Validation using the identified parameters with a different input voltage is illustrated in Fig. 8, achieving a fitness percentage of 85.95%. Furthermore, Fig. 9 shows the

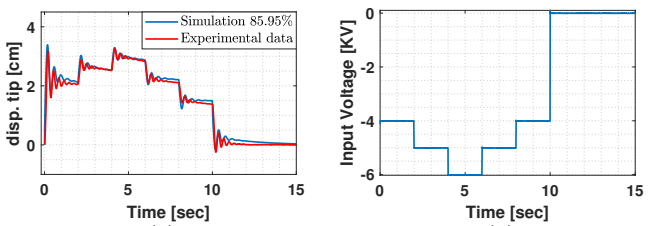

(a) (b)

Fig. 8. (8a) Model validation. (8b) Negative input signal.

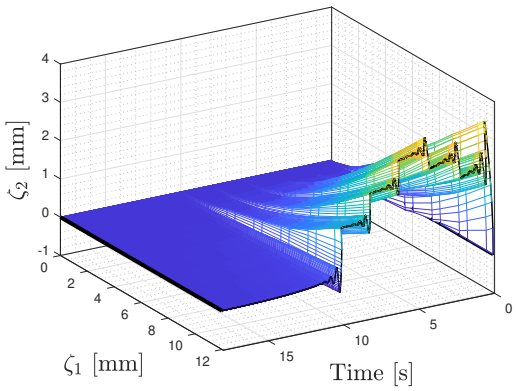

Fig. 9. Large-scale Curling HASEL model simulation.

evolution of the actuator profile for the input depicted in Fig. 8.b, where it is seen that the deformation profile is described properly and the model captures the drift effect in all the coordinates.

Discussion: Note that the structure of the large-scale model closely resembles that of the original low-scale model, implying that control strategies similar to those used in (Cisneros et al., 2024) could apply to this model. Additionally, the methodology offers a framework for modeling curling HASEL actuators, providing the flexibility to choose a beam model that accurately represents the behavior of the sheet that restricts deformation, including nonlinear options. Furthermore, the methodology suggests that chambers can be positioned at any point along the beam and actuated with different voltages, facilitating the modeling of continuous structures actuated with curling HASEL, suitable for robotics applications.

5. CONCLUSIONS

This paper proposes a methodology to extend the dynamics of a low-scale curling HASEL actuator by replacing the dynamics of the sheet that restricts the deformation with a discretized beam model. The resulting large-scale model has been experimentally validated, demonstrating satisfactory results and close alignment between simulations and the real system. Future work on this topic involves extending this approach to beams with multiple actuators to develop more complex deformation profiles. Additionally, it entails the development of control laws to stabilize the system around a desired deformed configuration, making it suitable for applications based on continuous deformation.

REFERENCES

Acome, E., Mitchell, S.K., Morrissey, T.G., Emmett, M.B., Benjamin, C., King, M., Radakovitz, M., and Keplinger, C. (2018). Hydraulically amplified self-healing electrostatic actuators with muscle-like performance. *Science*, 359(6371), 61–65.

Brugnoli, A., Rashad, R., Califano, F., Stramigioli, S., and Matignon, D. (2021). Mixed finite elements for port-Hamiltonian models of von Kármán beams. *IFAC-papersonline*, 54(19), 186–191.

Cisneros, N., Wu, Y., Rabenorosoa, K., and Le Gorrec, Y. (2024). Port-Hamiltonian modeling and control of a curling HASEL actuator. *https://hal.science/hal-04432915*.

Duindam, V., Macchelli, A., Stramigioli, S., and Bruyninckx, H. (2009). *Modeling and control of complex physical systems: the port-Hamiltonian approach*. Springer Science & Business Media.

Hainsworth, T., Schmidt, I., Sundaram, V., Whiting, G.L., Keplinger, C., and MacCurdy, R. (2022). Simulating electrohydraulic soft actuator assemblies via reduced order modeling. In *2022 IEEE 5th International Conference on Soft Robotics (RoboSoft)*, 21–28. IEEE.

Kellaris, N., Rothemund, P., Zeng, Y., Mitchell, S.K., Smith, G.M., Jayaram, K., and Keplinger, C. (2021). Spider-inspired electrohydraulic actuators for fast, soft-actuated joints. *Advanced Science*, 8(14), 2100916.

Kim, S. and Cha, Y. (2021). Double-layered electrohydraulic actuator for bi-directional bending motion of soft gripper. In *2021 18th International Conference on Ubiquitous Robots (UR)*, 645–649.

Macchelli, A. and Melchiorri, C. (2004). Modeling and control of the Timoshenko beam. the distributed port Hamiltonian approach. *SIAM journal on control and optimization*, 43(2), 743–767.

van der Schaft, A. (2000). *L2-gain and passivity techniques in nonlinear control*. Springer.

Volchko, A., Mitchell, S.K., Morrissey, T.G., and Humbert, J.S. (2022). Model-based data-driven system identification and controller synthesis framework for precise control of siso and miso HASEL-powered robotic systems. In *2022 IEEE 5th International Conference on Soft Robotics (RoboSoft)*, 209–216. IEEE.

Voß, T. and Scherpen, J.M. (2014). Port-Hamiltonian modeling of a nonlinear Timoshenko beam with piezo actuation. *SIAM Journal on Control and Optimization*, 52(1), 493–519.

Voss, T., Scherpen, J.M., and Onck, P.R. (2008). Modeling for control of an inflatable space reflector, the nonlinear 1-D case. In *2008 47th IEEE Conference on Decision and Control*, 1777–1782. IEEE.

Wang, M., Bestler, A., and Kotyczka, P. (2017). Modeling, discretization and motion control of a flexible beam in the port-Hamiltonian framework. *IFAC-PapersOnLine*, 50(1), 6799–6806.

Warsewa, A., Böhm, M., Sawodny, O., and Tarín, C. (2021). A port-Hamiltonian approach to modeling the structural dynamics of complex systems. *Applied Mathematical Modelling*, 89, 1528–1546.

Zienkiewicz, O.C., Taylor, R.L., and Zhu, J.Z. (2005). *The finite element method: Its basis and fundamentals*. Elsevier.